

Growth of $\text{CH}_3\text{NH}_3\text{PbI}_3$ cuboids with controlled size for high-efficiency perovskite solar cells

Jeong-Hyeok Im¹, In-Hyuk Jang¹, Norman Pellet^{2,3}, Michael Grätzel^{2*} and Nam-Gyu Park^{1*}

Perovskite solar cells with submicrometre-thick $\text{CH}_3\text{NH}_3\text{PbI}_3$ or $\text{CH}_3\text{NH}_3\text{PbI}_{3-x}\text{Cl}_x$ active layers show a power conversion efficiency as high as 15%. However, compared to the best-performing device, the average efficiency was as low as 12%, with a large standard deviation (s.d.). Here, we report perovskite solar cells with an average efficiency exceeding 16% and best efficiency of 17%. This was enabled by the growth of $\text{CH}_3\text{NH}_3\text{PbI}_3$ cuboids with a controlled size via a two-step spin-coating procedure. Spin-coating of a solution of $\text{CH}_3\text{NH}_3\text{I}$ with different concentrations follows the spin-coating of PbI_2 , and the cuboid size of $\text{CH}_3\text{NH}_3\text{PbI}_3$ is found to strongly depend on the concentration of $\text{CH}_3\text{NH}_3\text{I}$. Light-harvesting efficiency and charge-carrier extraction are significantly affected by the cuboid size. Under simulated one-sun illumination, average efficiencies of 16.4% (s.d. ± 0.35), 16.3% (s.d. ± 0.44) and 13.5% (s.d. ± 0.34) are obtained from solutions of $\text{CH}_3\text{NH}_3\text{I}$ with concentrations of 0.038 M, 0.050 M and 0.063 M, respectively. By controlling the size of the cuboids of $\text{CH}_3\text{NH}_3\text{PbI}_3$ during their growth, we achieved the best efficiency of 17.01% with a photocurrent density of 21.64 mA cm⁻², open-circuit photovoltage of 1.056 V and fill factor of 0.741.

Perovskite solar cells have recently attracted a great deal of attention because of their excellent photovoltaic performance, obtainable via a facile and cheap process. In the past two years, perovskite solar cells based on methylammonium lead halides have shown remarkable progress in terms of their power conversion efficiencies (PCEs). The introduction of $\text{CH}_3\text{NH}_3\text{PbX}_3$ ($X = \text{Br}, \text{I}$) by Miyasaka *et al.* as a sensitizer in an electrolyte-based dye-sensitized solar cell structure marked the beginning of perovskite-based photovoltaics^{1,2}. However, the perovskite sensitizer dissolved in the polar liquid electrolyte, leading to low PCEs of 3–6%. A report on a long-term durable 9.7% all-solid-state perovskite solar cell³ boosted research activities and, as a result, the PCE was quickly improved to 15% (refs 4–7). Certified PCEs for perovskite solar cells can be found at the National Renewable Energy Laboratory web site (http://www.nrel.gov/ncpv/images/efficiency_chart.jpg). The first version of the perovskite solar cell was based on the sensitizer concept, with $\text{CH}_3\text{NH}_3\text{PbI}_3$ (hereafter denoted MAPbI₃) perovskite nanodots formed on the TiO₂ surface³. It was found that the perovskite itself was able to transfer photo-excited electrons to the TiO₂, as confirmed by using an inert electron-blocking Al₂O₃ scaffold⁸. The surface sensitization concept subsequently evolved to an embodiment where the perovskite filled the mesoporous oxide structure, leading to a PCE of 12% (ref. 9). Structural modification from the sensitization³ of a nanocrystalline film to a planar junction⁵ was enabled by the balanced electron- and hole-transporting property of perovskite as well as a long diffusion length of more than 1 μm (refs 10–12).

Regarding the method to form perovskite MAPbI₃ inside the pores of the mesoporous TiO₂ (mp-TiO₂) film, a sequential two-step deposition has been proposed to obtain reproducible high-performance perovskite solar cells⁴. A PbI₂ solution was first spin-coated onto a mesoporous TiO₂ thin film, and the PbI₂-coated substrate was then immersed in a CH₃NH₃I solution. The highest PCE of 15% was achieved using the previous two-step deposition method⁴. A perovskite solar cell with vacuum-deposited

CH₃NH₃PbI_{3-x}Cl_x showed a best PCE of 15.4% (ref. 5). However, the average PCE was as low as 12% (ref. 4) and the standard deviation (s.d.) as large as ± 2.0 with the average PCE of 12.3% (ref. 5). Determining the correct efficiency of such planar perovskite devices is very difficult because of the notorious hysteresis effects in the *J-V* curves. Thus, a reproducible and efficient way for realizing perovskite photovoltaics with an average PCE above 15%, as well as a small s.d., is required.

Here, we report high-efficiency perovskite solar cells with an average PCE exceeding 16% with small s.d. (less than 0.4), together with a best PCE of 17%, by size-controlled growth of MAPbI₃ cuboids. MAPbI₃ crystals were grown by two-step spin-coating procedure and the size of the cuboids was controlled with the CH₃NH₃I solution concentration.

Growth of $\text{CH}_3\text{NH}_3\text{PbI}_3$ cuboids with controlled size

The two-step spin-coating procedure is described schematically in Fig. 1. Mesoporous TiO₂ (~ 40 nm in diameter) film was deposited on a thin compact TiO₂ blocking layer, followed by spin-coating 20 μl of a 1 M solution of PbI₂ in *N,N*-dimethylformamide (DMF). In the second step, a 200 μl (8 $\mu\text{l cm}^{-2}$) CH₃NH₃I solution was spin-coated onto the dried PbI₂ film and then dried at 100 °C to form MAPbI₃. A loading time of 20 s before spinning is required for the CH₃NH₃I coating, but no loading time is needed for the PbI₂ coating. The concentration of CH₃NH₃I solution was varied from 0.038 M (6 mg of CH₃NH₃I in 1 ml 2-propanol) to 0.063 M (10 mg l⁻¹) (0.063 M was used in the previous report⁴). The present two-step spin-coating method is expected to be more precise than the two-step dipping method^{4,13} because of its quantitatively managed procedure.

We find that the two-step spin-coating procedure leads to the formation of MAPbI₃ cuboids and that the size and shape of these cuboids are greatly influenced by CH₃NH₃I concentration. As confirmed by the scanning electron microscopy (SEM) images in Fig. 2a–e, the size of the MAPbI₃ cuboids increases with

¹School of Chemical Engineering and Department of Energy Science, Sungkyunkwan University, Suwon 440-746, Korea, ²Laboratory for Photonics and Interfaces, Institute of Chemical Sciences and Engineering, School of Basic Sciences, Ecole Polytechnique Fédérale de Lausanne, CH-1015 Lausanne, Switzerland, ³Max-Planck-Institute for Solid-State Research, Heisenbergstrasse 1, 70569 Stuttgart, Germany. *e-mail: npark@skku.edu; michael.gratzel@epfl.ch

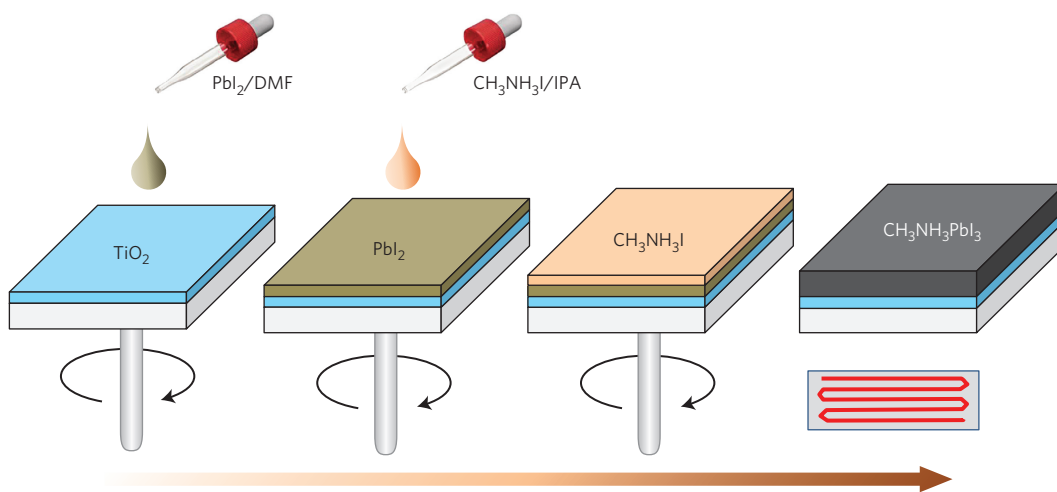


Figure 1 | Two-step spin-coating procedure for $\text{CH}_3\text{NH}_3\text{PbI}_3$ cuboids. A 1 M PbI_2 solution is spin-coated onto the mesoporous TiO_2 film. The PbI_2 -coated film is dried at 40 °C for 3 min and 100 °C for 5 min. A $\text{CH}_3\text{NH}_3\text{I}$ solution is then loaded onto this for 20 s and spun. Finally, the film is heated at 100 °C for 5 min. The concentrations of the $\text{CH}_3\text{NH}_3\text{I}$ solution in 2-propanol are 0.038 M (6 mg ml^{-1}), 0.044 M (7 mg ml^{-1}), 0.050 M (8 mg ml^{-1}), 0.057 M (9 mg ml^{-1}) or 0.063 M (10 mg ml^{-1}).

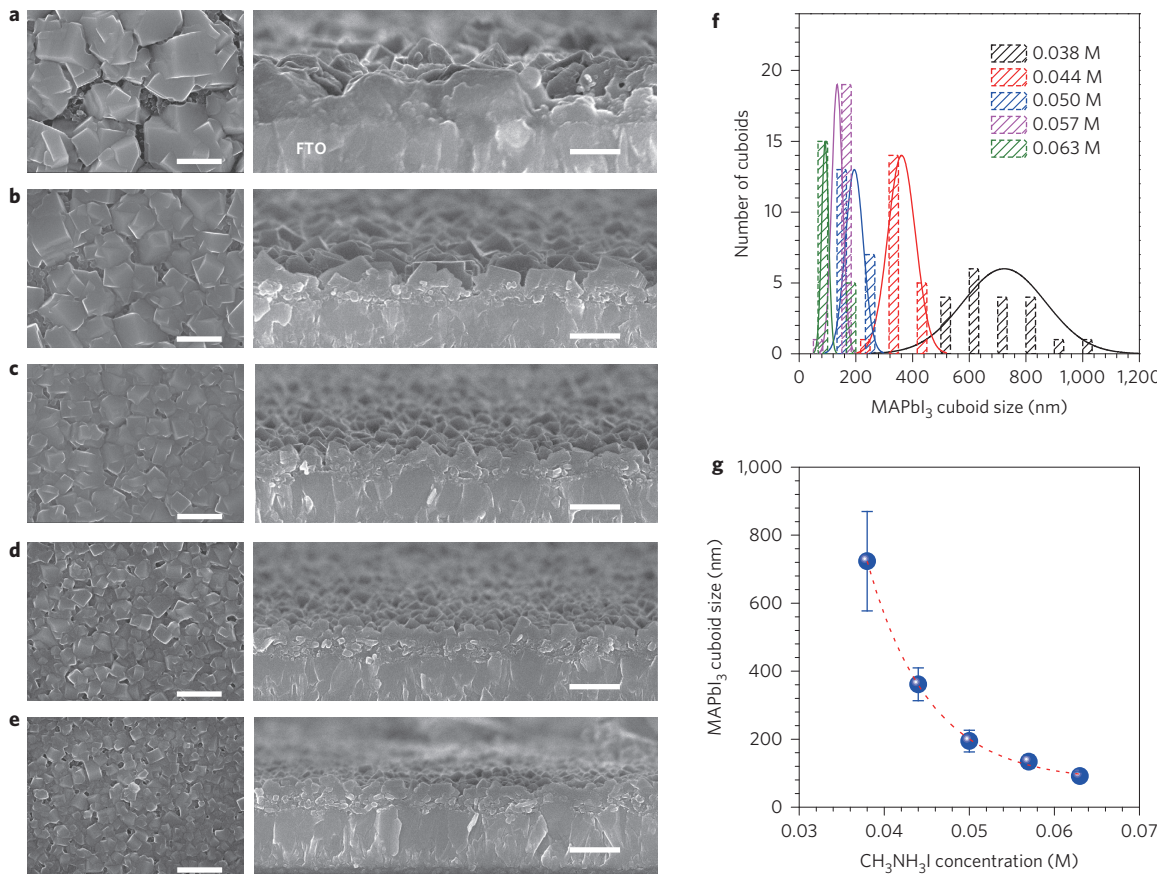


Figure 2 | Surface cross-sectional scanning electron microscopy images and dependence of MAPbI_3 cuboid size on $\text{CH}_3\text{NH}_3\text{I}$ concentration. **a–e**, Surface (left) and cross-sectional (right) SEM images of MAPbI_3 cuboids grown on a mesoporous TiO_2 layer by the two-step spin-coating procedure from $\text{CH}_3\text{NH}_3\text{I}$ concentrations of 0.038 M (**a**), 0.044 M (**b**), 0.050 M (**c**), 0.057 M (**d**) and 0.063 M (**e**). Scale bars, 500 nm. **f**, Histogram of MAPbI_3 cuboid size for $\text{CH}_3\text{NH}_3\text{I}$ concentrations from 0.038 M to 0.063 M. Solid lines represent normal distribution curves. **g**, Plot of average MAPbI_3 cuboid size versus $\text{CH}_3\text{NH}_3\text{I}$ concentration. Data (blue circles) were fit with a nonlinear curve with asymptotic exponential relation (dashed red line). Error bars represent s.d. FTO, fluorine-doped tin oxide.

decreasing $\text{CH}_3\text{NH}_3\text{I}$ concentration. The average cuboid size is determined to be $\sim 720 \text{ nm}$ for 0.038 M, $\sim 360 \text{ nm}$ for 0.044 M, $\sim 190 \text{ nm}$ for 0.050 M, $\sim 130 \text{ nm}$ for 0.057 M and $\sim 90 \text{ nm}$ for

0.063 M. From the cross-sectional SEM images, the thickness of the cuboids is $\sim 300\text{--}400 \text{ nm}$, indicating that the growth rate along the *c*-axis is slower than in the *a*- and *b*-axes directions for the

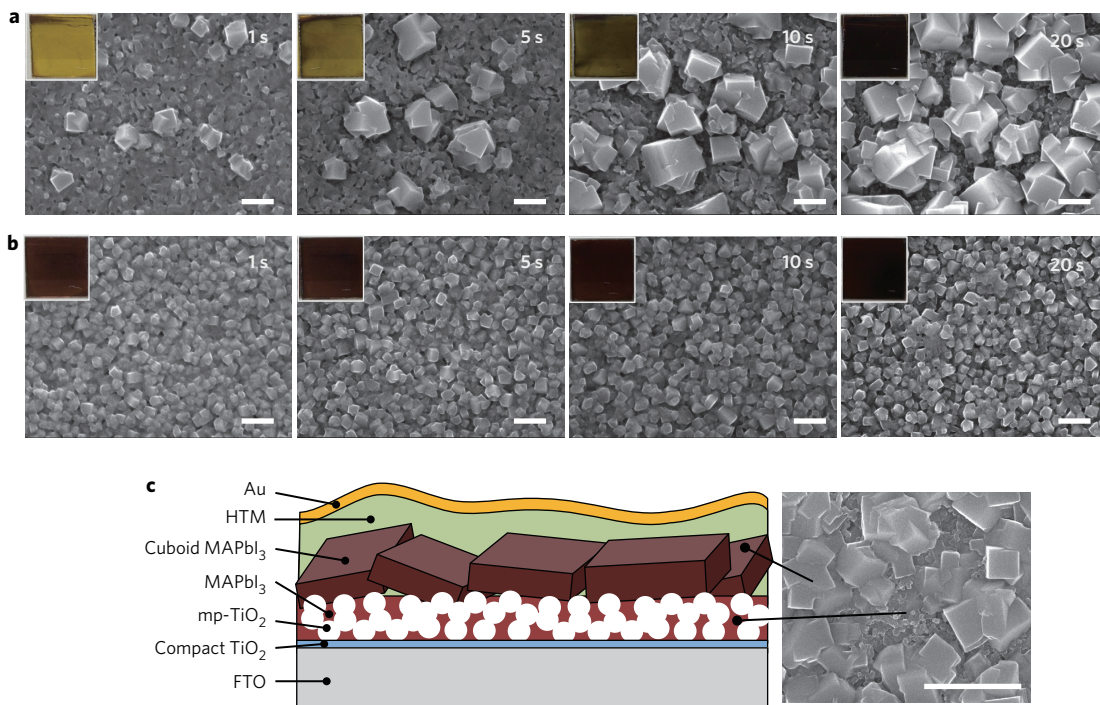


Figure 3 | **MAPbI₃ nucleation, crystal growth and cell configuration.** **a,b,** Surface scanning electron microscopy (SEM) images at different loading times for the 0.038 M (**a**) and 0.063 M (**b**) $\text{CH}_3\text{NH}_3\text{I}$ solutions. Samples for SEM were prepared as follows: $\text{CH}_3\text{NH}_3\text{I}$ solution (100 μl) was loaded onto the PbI_2 -coated substrate, left (loading time) for 1 s, 5 s, 10 s and 20 s, spun at 4,000 r.p.m. for 20 s, and finally heated at 100 °C for 5 min. MAPbI_3 perovskite was grown on the mesoporous TiO_2 layer (mp- TiO_2). Insets: Photographs of the samples used for SEM measurement. Scale bars, 500 nm. **c,** Schematic of the perovskite solar cell configuration based on surface and cross-sectional SEM images, where large cuboid MAPbI_3 was formed on top of the mesoporous TiO_2 layer. Scale bar (SEM image), 1 μm . FTO, fluorine-doped tin oxide; HTM, hole-transport material.

lowest concentration of 0.038 M. The size distribution broadens (narrows) as the $\text{CH}_3\text{NH}_3\text{I}$ concentration decreases (increases), as shown in Fig. 2f. MAPbI_3 cuboid size is plotted as a function of $\text{CH}_3\text{NH}_3\text{I}$ concentration in Fig. 2g, which shows an exponential decay of cuboid size with $\text{CH}_3\text{NH}_3\text{I}$ concentration. An exponential function to an asymptotic plateau gives a good fit for the data, suggesting that the MAPbI_3 crystal growth strongly correlates with $\text{CH}_3\text{NH}_3\text{I}$ concentration. We further extended our analysis to lower concentrations, such as 0.032 M (5 mg ml⁻¹). Supplementary Fig. 1 compares perovskite cuboids grown from a concentration of 0.032 M with those from 0.038 M. A longer loading time is required for the lower concentration of 0.032 M (loading time 60 s). The lower concentration leads to bigger cuboid size, with average dimension exceeding 1 μm . The perovskite cuboid size can therefore be derived from the extrapolation of the exponential curve in Fig. 2g.

The perovskite cuboids are much larger than TiO_2 nanoparticles (~40 nm), so perovskite is not a thin conformal layer covering the TiO_2 particles sandwiched with spiro-MeOTAD. As can be seen in Supplementary Fig. 2, the TiO_2 pores are filled with PbI_2 , and a capping layer of PbI_2 is also formed during the first coating step. During the second step of the coating procedure, all the PbI_2 is converted to perovskite, as confirmed by X-ray diffraction (XRD) (data not shown). The perovskite therefore forms not only inside the TiO_2 pores, but also on top of the TiO_2 layer. Due to the pore size of the TiO_2 film, the growth of perovskite is limited inside the pores, whereas larger crystal growth is possible on top of the TiO_2 film. A cross-sectional SEM of the full cell (Supplementary Fig. 3) shows that the size of the perovskite cuboids affects the roughness of the spiro-MeOTAD and Au layers. Both become rougher on contact with large-sized cuboids. Although the layer structure is expected to influence the PCE, the perovskite morphology is eventually found to play a more important role in a given cell structure.

Growth mechanism of $\text{CH}_3\text{NH}_3\text{PbI}_3$ cuboids

We investigated the change in surface morphology as a function of the loading time of the $\text{CH}_3\text{NH}_3\text{I}$ solution onto the PbI_2 -infiltrated scaffold to further scrutinize the dependence of MAPbI_3 cuboid size on $\text{CH}_3\text{NH}_3\text{I}$ concentration, as well as crystal growth behaviour. To track the crystal growth, SEM images were monitored at different loading time: 1 s, 5 s, 10 s and 20 s. Samples for the SEM images (for different loading times) in Fig. 3 were prepared as follows. For the crystal growth study, 100 μl $\text{CH}_3\text{NH}_3\text{I}$ solution was loaded on the PbI_2 -coated TiO_2 scaffold, followed by a waiting period of 1 s, 5 s, 10 s or 20 s (20 s is experimental condition). At this stage, the samples were spun at 4,000 r.p.m. for 20 s and then finally heated at 100 °C for 5 min. Crystal growth with waiting time is evident for the 0.038 M $\text{CH}_3\text{NH}_3\text{I}$ solution, whereas no crystal growth occurred with time for the higher concentration of 0.063 M. For 0.038 M, the growth in size is rendered possible by the low $\text{CH}_3\text{NH}_3\text{I}$ concentration, because the seed crystals are sparsely distributed (Fig. 3a). This is also indicative of localized nucleation. In contrast to the low concentration case, further crystal growth is inhibited at the higher concentration because nucleation and growth are already terminated at the initial stage (1 s), as can be seen in Fig. 3b. The colour turned from light brown to dark black for the 0.038 M case, but no change in colour was observed for the 0.063 M case, supporting the notion that there is an important difference in nuclei density. Absorption near the bandgap was found to increase with cuboid size, as confirmed by the absorption coefficient, which was evaluated from transmittance and reflectance measurements using an integrating sphere (Supplementary Fig. 4).

Size-dependent photovoltaic characteristics

Figure 4 demonstrates that the photovoltaic performance is strongly influenced by $\text{CH}_3\text{NH}_3\text{I}$ concentration. For the 0.038 M case, the average values (with s.d.) for short-circuit current density J_{sc} , open-

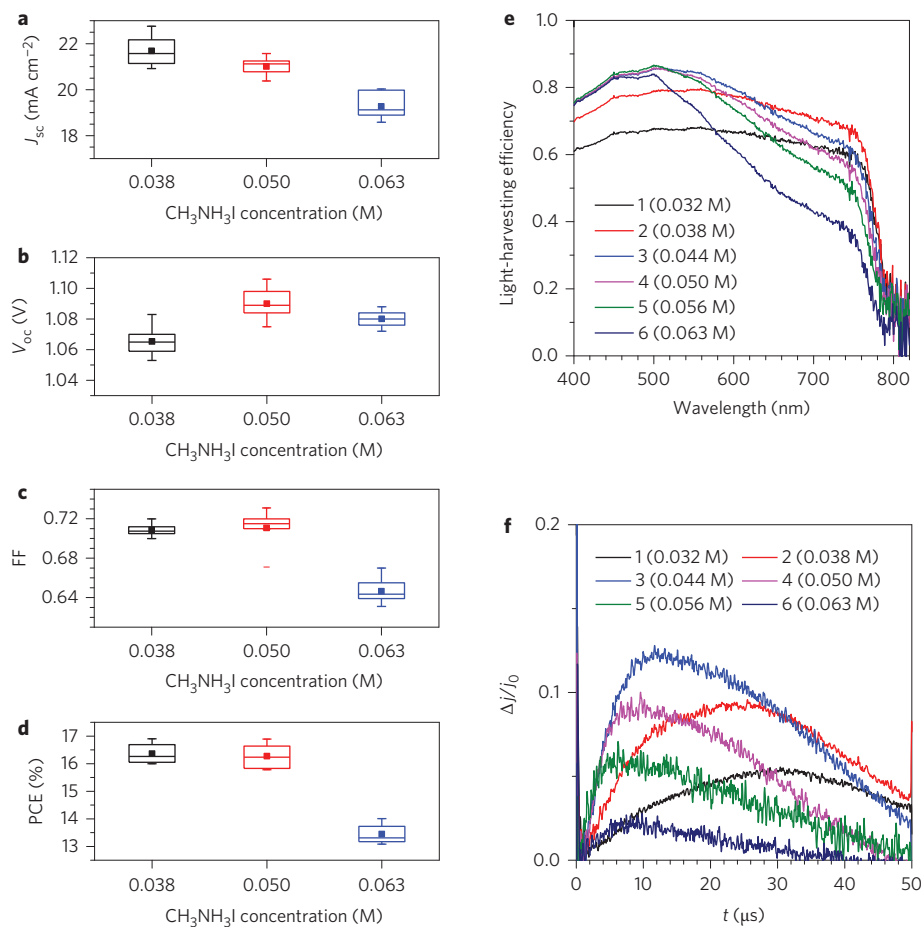


Figure 4 | Effects of MAPbI_3 cuboid size on photovoltaic parameters, light-harvesting efficiency and photo-CELIV transients. **a-d**, Short-circuit current density J_{sc} , open-circuit voltage V_{oc} , fill factor (FF) and power conversion efficiency (PCE) versus $\text{CH}_3\text{NH}_3\text{I}$ concentration. Error bars represent minimum and maximum values, and the middle line in each box represents the median value. Upper and lower error bars in the box represent the third quartile (Q3) and first quartile (Q1), respectively, and box thickness represents interquartile Q3-Q1. Filled squares indicate mean values. Detailed statistics are shown in Supplementary Tables 1–3. **e**, Light-harvesting efficiency spectra of the MAPbI_3 films depending on $\text{CH}_3\text{NH}_3\text{I}$ concentration. **f**, Photo-CELIV transients recorded for devices comprising FTO/bl-Al₂O₃/mp-TiO₂/ MAPbI_3 /spiro-MeOTAD/Au depending on $\text{CH}_3\text{NH}_3\text{I}$ concentration. j , current; Δj , extraction current; j_0 , capacitive displacement current.

circuit voltage V_{oc} , fill factor (FF) and PCE are $21.68 \pm 0.63 \text{ mA cm}^{-2}$, $1.065 \pm 0.009 \text{ V}$, 0.709 ± 0.006 and $16.36 \pm 0.35\%$, respectively (Supplementary Table 1). A J_{sc} of $21.01 \pm 0.37 \text{ mA cm}^{-2}$, V_{oc} of $1.090 \pm 0.009 \text{ V}$, FF of 0.711 ± 0.017 and PCE of $16.27 \pm 0.44\%$ were achieved as average values for 0.050 M $\text{CH}_3\text{NH}_3\text{I}$ (Supplementary Table 2). Compared to low concentrations, a smaller PCE of $13.45 \pm 0.55\%$ is obtained from the 0.063 M $\text{CH}_3\text{NH}_3\text{I}$ solution, as well as a J_{sc} of $19.27 \pm 0.55 \text{ mA cm}^{-2}$, V_{oc} of $1.080 \pm 0.005 \text{ V}$ and FF of 0.646 ± 0.012 (Supplementary Table 3). As can be seen in Fig. 4a, J_{sc} gradually declines with increasing $\text{CH}_3\text{NH}_3\text{I}$ concentration. The higher J_{sc} at the lower concentration might be due to light scattering by the larger-sized MAPbI_3 cuboids. Light-harvesting efficiency is measured and compared in Fig. 4e. These spectra indicate that, for samples with lower $\text{CH}_3\text{NH}_3\text{I}$ concentrations, the crystals formed are bigger, as evidenced by the flatter profiles. However, spacing between the crystals contributes to the lower light-harvesting efficiency for samples 1 (0.032 M) and 2 (0.038 M), and all gaps seem to be closed for the samples processed at higher $\text{CH}_3\text{NH}_3\text{I}$ concentrations. As the concentration is increased, internal scattering is decreased, which shows up as a decrease in the green-red region. The baseline above the bandgap is attributed to the specular reflectance of the TiO_2 /perovskite interface, which has not been subtracted. Overall, samples 2 and 3 (0.044 M) show the greatest light harvesting. Change in size of MAPbI_3 is

likely to affect charge extraction behaviour, which also affects the photocurrent. Measurements of charge carrier extraction by linearly increasing the voltage under illumination (photo-CELIV)¹⁴ were carried out in ambient air over FTO/bl-Al₂O₃/mp-TiO₂/ MAPbI_3 /spiro-MeOTAD/Au assemblies, where a blocking Al₂O₃ underlayer (bl-Al₂O₃) on a fluorine-doped tin oxide (FTO) was used to prevent electron collection. Hence, only the holes were collected at the back contact. The photo-CELIV transients are shown in Fig. 4f. The data show that smaller crystals demonstrate the fastest extraction rate, which is related to a higher hole mobility, assuming a similar film thickness. However, the total amount of extracted charge is maximal for the 0.044 M $\text{CH}_3\text{NH}_3\text{I}$ solution. At lower and higher concentrations, the amount of extracted charges is lower, partly due to the decreased light harvesting, but also due to faster recombination, which is responsible for broadening of the signal. The photogenerated current never exceeds 20% of the capacitive current, so the space-charge effects are considered minimal. The slower recombination in films with intermediate crystal sizes prevails over the increased hole mobility measured for the smaller crystals. We observe that the optimum crystal size is due to a synergy of light-harvesting and carrier-extraction effects. Further investigations in that regard are currently ongoing.

V_{oc} is higher for the 0.050 M methylammonium iodide concentration than for the 0.038 M and 0.063 M concentrations (Fig. 4b).

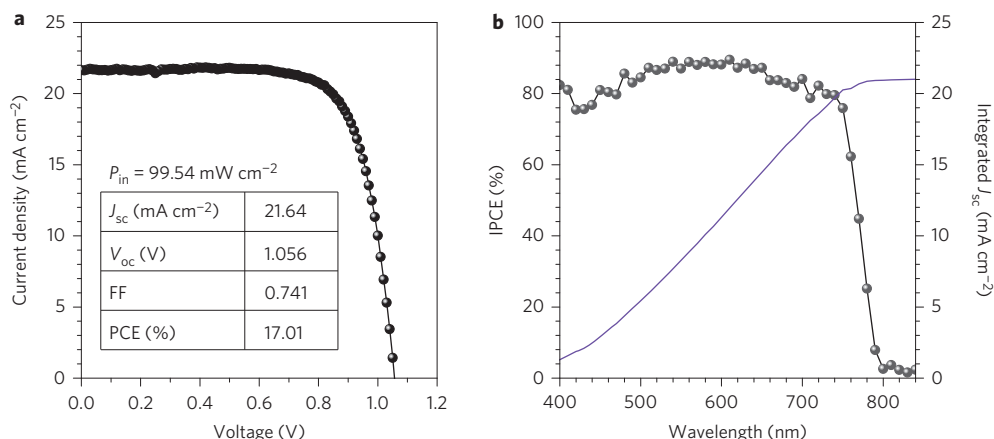


Figure 5 | Current density-voltage curve and incident photon-to-electron conversion efficiency values for the best-performing device. **a**, Current density–voltage curve measured under AM 1.5G condition with input solar power P_{in} of 99.54 mW cm^{-2} . **b**, Incident photon-to-electron conversion efficiency (IPCE) spectrum (black circles and line) and integrated photocurrent density J_{sc} (purple line) for the best-performing perovskite solar cell with MAPbI_3 formed from $0.038 \text{ M CH}_3\text{NH}_3\text{I}$. Integrated J_{sc} was calculated to be 21 mA cm^{-2} . Aperture cell area was 0.159 cm^2 . IPCE data were collected under the AC mode under 10% of full sun as the bias light intensity.

As mentioned above in connection with the photo-CELIV transient study, a change in V_{oc} correlates with the rate of charge carrier extraction and recombination. Because light-harvesting efficiency and the amount of extracted charges deteriorated despite a further increase in cuboid size formed from the $0.032 \text{ M CH}_3\text{NH}_3\text{I}$ concentration, we investigated the photovoltaic performance of a device comprising very large cuboid MAPbI_3 formed from the $0.032 \text{ M CH}_3\text{NH}_3\text{I}$. As expected, both the V_{oc} and J_{sc} declined, to 0.923 V and 17 mA cm^{-2} , respectively (Supplementary Fig. 5), confirming that an intermediate cuboid size is optimal for obtaining high photovoltaic performance as a result of excellent light harvesting and charge carrier extraction.

The highest V_{oc} of 1.106 V was observed from the $0.050 \text{ M CH}_3\text{NH}_3\text{I}$ solution. Compared to the high FF values of over 0.7 for the 0.038 M and $0.050 \text{ M CH}_3\text{NH}_3\text{I}$, the MAPbI_3 prepared from the $0.063 \text{ M CH}_3\text{NH}_3\text{I}$ shows a relatively low FF (Fig. 4c), which is probably due to the increased number of grain boundaries in the MAPbI_3 layer that the charge carriers have to cross with smaller cuboids. This is expected to increase the series resistance, leading to a low FF. Series resistance R_s is estimated from the measured J – V curves using the diode equation (equation (1)), where ideal diode behaviour ($n=1$) is assumed and I_L , I_0 , q , k , T and V represent photocurrent, inverse polarization dark saturation current, charge, Boltzmann constant, absolute temperature and bias potential, respectively:

$$I = I_L - I_0 \exp\left(\frac{q(V + IR_s)}{nkT}\right) \quad (1)$$

R_s was estimated to be 4.77 , 4.85 and $8.51 \Omega \text{ cm}^2$ for 0.038 , 0.050 and $0.063 \text{ M CH}_3\text{NH}_3\text{I}$, respectively. R_s increases substantially as $\text{CH}_3\text{NH}_3\text{I}$ concentration increases (cuboid size decreases), which correlates with the observed decrease in fill factor. The change in series resistance is likely to be related to perovskite structure. It has been reported that in heterostructure solar cells, grain boundaries have an influence on photovoltaic parameters, and series resistance can increase with number of grain boundaries¹⁵. The high fill factors observed for large-sized perovskites formed at low $\text{CH}_3\text{NH}_3\text{I}$ concentrations are ascribed to the low series resistance, probably as a result of there being fewer grain boundaries.

The integrated J_{sc} values based on incident photon-to-electron conversion efficiency (IPCE) data are found to be consistent with the J_{sc} values obtained from a solar simulator, as shown in Supplementary Fig. 6. This shows that the spectral mismatch between the simulator and the AM 1.5 standard solar emission is negligibly small. The average PCEs are similar for 0.038 M and

$0.050 \text{ M CH}_3\text{NH}_3\text{I}$ (Fig. 4d). The high average PCE of 16.4% is mainly ascribed to the high J_{sc} for $0.038 \text{ M CH}_3\text{NH}_3\text{I}$, and the high PCE of 16.3% for the $0.050 \text{ M CH}_3\text{NH}_3\text{I}$ is mainly due to the larger V_{oc} . The photovoltaic performances for the intermediate concentrations of 0.044 M and 0.057 M were also studied, and the photovoltaic parameters of those devices were found to be in good agreement with the overall trend (Supplementary Figs 7 and 8). Because the loading time of $\text{CH}_3\text{NH}_3\text{I}$ may affect the size of the perovskite cuboids and thereby photovoltaic performance, the loading time was varied from 20 s to 60 s at a concentration of 0.038 M . Little change in cuboid size or photovoltaic performance was observed, as can be seen in Supplementary Fig. 9, which indicates that crystal growth is complete by 20 s , and prolonged loading for 60 s would not deteriorate the photovoltaic performance.

It has been argued that perovskite solar cells exhibit I – V hysteresis^{16–18}, so I – V measurements were performed versus scan direction (Supplementary Fig. 10). Little I – V hysteresis is observed for the $\text{CH}_3\text{NH}_3\text{PbI}_3$ grown at concentrations of 0.038 M and 0.050 M , whereas hysteresis cannot be ignored for the higher concentration of 0.068 M , which indicates that large crystals are better for tolerating I – V hysteresis. Further study on the basis for size-dependent I – V hysteresis is under way.

The highest PCE of 17.01% was achieved using $0.038 \text{ M CH}_3\text{NH}_3\text{I}$, yielding a J_{sc} of 21.64 mA cm^{-2} , V_{oc} of 1.056 V , and FF of 0.741 (Fig. 5). The integrated J_{sc} of 21 mA cm^{-2} from IPCE data agrees well with the measured value. To the best of our knowledge, this strikingly high PCE of 17% is a record efficiency for MAPbI_3 -based perovskite solar cells.

Conclusions

By using a two-step spin-coating procedure, we have developed a reproducible method for preparing MAPbI_3 -based perovskite solar cells with the highest efficiencies yet reported. This method yields a s.d. of less than 0.4 and an average PCE as high as 16.4% . Optimizing the size of MAPbI_3 cuboids in the capping layer was key to obtain high light harvesting and charge carrier extraction. We found that the size of the cuboids was very strongly dependent on $\text{CH}_3\text{NH}_3\text{I}$ concentration and the exposure time of the PbI_2 to the $\text{CH}_3\text{NH}_3\text{I}$ solution before spin coating. Photovoltaic parameters were also significantly dependent on $\text{CH}_3\text{NH}_3\text{I}$ concentration because of the difference in crystal size of the MAPbI_3 . From the size-controlled growth of MAPbI_3 , cuboids grown from two-step spin coating with $\text{CH}_3\text{NH}_3\text{I}$ concentrations higher than 0.038 M and less than 0.050 M are required to yield a PCE of 17% .

Methods

Synthesis of $\text{CH}_3\text{NH}_3\text{I}$. Methylamine (27.86 ml, 40% in methanol, TCI) and hydroiodic acid (30 ml, 57 wt% in water, Aldrich) were mixed at 0 °C and stirred for 2 h. The precipitate was recovered by evaporation at 50 °C for 1 h. The product was washed with diethyl ether three times and finally dried at 60 °C in a vacuum oven for 24 h.

Preparation of TiO_2 paste. Anatase TiO_2 nanoparticles (diameter of ~40 nm) were synthesized using a two-step hydrothermal method. The seed particles (diameter of ~20 nm) were synthesized by acetic-acid-catalysed hydrolysis of titanium isopropoxide (97%, Aldrich) and autoclaving at 230 °C for 12 h. The seed particles were washed with ethanol and collected by centrifugation. Hydrothermal treatment was performed again with the seed particles to grow in size. TiO_2 paste was prepared by mixing the TiO_2 particles (~40 nm) with terpineol (EC, 99.5%, Aldrich), ethyl cellulose (EC, 46 cp, Aldrich) and lauric acid (LA, 96%, Fluka) at a nominal ratio of $\text{TiO}_2:\text{TP:EC:LA} = 1.25:6.0:6.0:1$. The paste was further treated with a three-roll mill for 40 min.

Solar cell fabrication. FTO glasses (Pilkington, TEC-8, 8 Ω sq⁻¹) were cleaned in an ultrasonic bath containing ethanol for 20 min, and treated in a UV Ozone (UVO) cleaner for 20 min. The TiO_2 blocking layer (BL) was spin-coated on an FTO substrate at 2,000 r.p.m. for 20 s using 0.15 M titanium diisopropoxide bis (acetylacetone) (75 wt% in isopropanol, Aldrich) in 1-butanol (99.8%, Aldrich) solution, which was heated at 125 °C for 5 min. After cooling to room temperature, the TiO_2 paste was spin-coated on the BL layer at 2,000 r.p.m. for 10 s, where the pristine paste was diluted in ethanol (0.1 g ml⁻¹). After drying at 100 °C for 5 min, the film was annealed at 550 °C for 30 min, providing a thickness of ~100 nm. The mesoporous TiO_2 film was immersed in 0.02 M aqueous TiCl_4 (>98%, Aldrich) solution at 90 °C for 10 min. After washing with deionized water and drying, the film was heated at 500 °C for 30 min. $\text{CH}_3\text{NH}_3\text{PbI}_3$ was formed using two-step spin-coating procedure. PbI_2 solution (1 M) was prepared by dissolving 462 mg PbI_2 (99%, Aldrich) in 1 ml *N,N*-dimethylformamide (DMF, 99.8%, Sigma-Aldrich) under stirring at 70 °C. PbI_2 solution (20 μl) was spin-coated on the mesoporous TiO_2 film at 3,000 r.p.m. for 5 s and 6,000 r.p.m. for 5 s (without loading time). After spinning, the film was dried at 40 °C for 3 min and then 100 °C for 5 min, and after cooling to room temperature, 200 μl of 0.038 M (6 mg ml⁻¹), 0.044 M (7 mg ml⁻¹), 0.050 M (8 mg ml⁻¹), 0.057 M (9 mg ml⁻¹) or 0.063 M (10 mg ml⁻¹) $\text{CH}_3\text{NH}_3\text{I}$ solution in 2-propanol was loaded on the PbI_2 -coated substrate for 20 s (loading time), which was spun at 4,000 r.p.m. for 20 s and dried at 100 °C for 5 min. A volume of 20 μl of 2,2',7,7'-tetrakis(*N,N*-di-*p*-methoxyphenylamine)-9,9'-spirobifluorene (spiro-MeOTAD) solution was spin-coated on the $\text{CH}_3\text{NH}_3\text{PbI}_3$ perovskite layer at 4,000 r.p.m. for 30 s. A spiro-MeOTAD solution was prepared by dissolving 72.3 mg of spiro-MeOTAD in 1 ml of chlorobenzene, to which 28.8 μl of 4-*tert*-butyl pyridine and 17.5 μl of lithium bis(trifluoromethanesulfonyl)imide (Li-TFSI) solution (520 mg Li-TFSI in 1 ml acetonitrile, Sigma-Aldrich, 99.8%) were added. Finally, 80 nm of gold was thermally evaporated on the spiro-MeOTAD-coated film.

Device characterization. Photocurrent and voltage were measured with a solar simulator equipped with 450 W xenon lamp (Newport 6279 NS) and a Keithley 2400 source meter. Light intensity was adjusted with an NREL-calibrated Si solar cell with a KG-2 filter for approximating 1 sun light intensity (100 mW cm⁻²). While measuring current and voltage, the cell was covered with a black mask with an aperture (aperture area is close to the active device area). IPCE spectra were recorded as functions of wavelength in the alternating current (AC) mode under a constant white light bias of ~10 mW cm⁻², supplied by an array of white-light-emitting diodes. The excitation beam coming from a 300 W xenon lamp (ILC Technology) was focused through a Gemini-180 double monochromator (Jobin Yvon) and chopped at ~2 Hz. The signal was recorded using a Model SR830 DSP lock-in amplifier (Stanford Research Systems). All measurements were conducted using a non-reflective metal aperture of 0.159 cm² to define the active area of the device and avoid light scattering through the sides. A field-emission scanning electron microscope (FE-SEM, Jeol JSM 6700F) was used to investigate the surface and cross-sectional morphology of the perovskite solar cells.

Light-harvesting efficiency measurement. To measure the light-harvesting efficiency of the films, 1.3 × 1.4 cm FTO/mesoporous $\text{TiO}_2/\text{MAPbI}_3$ films were placed in the centre of a 102-mm-diameter integrated sphere (Horiba F-3018). Measurements were conducted in a spectrophotometer (Fluorolog 322, Horiba Jobin Yvon). Samples were illuminated by a 450 W xenon lamp through a double monochromator (slit width of 0.5 mm) directed into the sphere. The outgoing light was measured at 90° from the entry aperture through a neutral density filter (0.5%). The samples were measured successively at 90° and 0° from the incoming light. The spectra were photometrically corrected. The emission monochromator was scanned synchronously with the excitation monochromator. A blank spectrum consisting of FTO/ TiO_2 only was measured and subtracted.

Photo-CELIV measurements. Photo-CELIV was conducted on FTO/b-Al₂O₃/m-TiO₂/MAPbI₃/spiro-MeOTAD/Au devices in ambient air. The Al₂O₃ underlayer (b-Al₂O₃) was used to block electron collection, hence leading to the collection of only holes. The active area was defined by the size of the counter-electrode (0.56 cm²). A 4 ns laser pulse provided by a frequency-doubled Nd:YAG laser (Ekspla NT 342/3(UV)) at 532 nm was diverged through a BK7 lens and directed towards the sample. After a delay of 150 μs, during which the device was left without

external bias, a linearly increasing voltage ramp was applied to the sample (10 V over 50 μs) to extract the positive charge carriers. A Tektronix AFG2021 function generator provided the delay and the voltage pulse. The signal was grounded through a 5 Ω load resistance, across which the current was measured (Tektronix DPO 7104C). The pulse sequence was repeated 18 times. The first extraction pulse was used to measure photogenerated carriers and the last pulse to provide the dark capacitance current. All traces were corrected for their *y*-offset due to deviations in dark carrier concentrations between the first and last pulse.

Received 7 February 2014; accepted 30 July 2014;
published online 31 August 2014

References

- Kojima, A., Teshima, K., Shirai, Y. & Miyasaka, T. Organometal halide perovskites as visible-light sensitizers for photovoltaic cells. *J. Am. Chem. Soc.* **131**, 6050–6051 (2009).
- Im, J.-H., Lee, C.-R., Lee, J.-W., Park, S.-W. & Park, N.-G. 6.5% efficient perovskite quantum-dot-sensitized solar cell. *Nanoscale* **3**, 4088–4093 (2011).
- Kim, H.-S. *et al.* Lead iodide perovskite sensitized all-solid-state submicron thin film mesoscopic solar cell with efficiency exceeding 9%. *Sci. Rep.* **2**, 591 (2012).
- Burschka, J. *et al.* Sequential deposition as a route to high-performance perovskite-sensitized solar cells. *Nature* **499**, 316–319 (2013).
- Liu, M., Johnston, M. B. & Snaith, H. J. Efficient planar heterojunction perovskite solar cells by vapour deposition. *Nature* **501**, 395–398 (2013).
- Wojciechowski, K., Saliba, M., Leijtens, T., Abate, A. & Snaith, H. J. Sub-150 °C processed meso-superstructured perovskite solar cells with enhanced efficiency. *Energy Environ. Sci.* **7**, 1142–1147 (2014).
- Wang, J. T.-W. *et al.* Low-temperature processed electron collection layers of graphene/TiO₂ nanocomposites in thin film perovskite solar cells. *Nano Lett.* **14**, 724–730 (2014).
- Lee, M. M., Teuscher, J., Miyasaka, T., Murakami, T. N. & Snaith, H. J. Efficient hybrid solar cells based on meso-superstructured organometal halide perovskites. *Science* **338**, 643–647 (2012).
- Heo, J. H. *et al.* Efficient inorganic–organic hybrid heterojunction solar cells containing perovskite compound and polymeric hole conductors. *Nature Photon.* **7**, 486–491 (2013).
- Xing, G. *et al.* Long-range balanced electron- and hole-transport length in organic–inorganic $\text{CH}_3\text{NH}_3\text{PbI}_3$. *Science* **342**, 344–347 (2013).
- Stranks, S. D. *et al.* Electron–hole diffusion lengths exceeding 1 micrometer in an organometal trihalide perovskite absorber. *Science* **342**, 341–344 (2013).
- Gonzalez-Pedro, V. *et al.* General working principles of $\text{CH}_3\text{NH}_3\text{PbX}_3$ perovskite solar cells. *Nano Lett.* **14**, 888–893 (2014).
- Liang, K., Mitzi, D. B. & Prikas, M. T. Synthesis and characterization of organic–inorganic perovskite thin films prepared using a versatile two-step dipping technique. *Chem. Mater.* **10**, 403–411 (1998).
- Juška, G., Arlauskas, K., Viliūnas, M. & Kočka, J. Extraction current transients: new method of study of charge transport in microcrystalline silicon. *Phys. Rev. Lett.* **84**, 4946–4949 (2000).
- Fraas, L. M. Basic grain-boundary effects in polycrystalline heterostructure solar cells. *J. Appl. Phys.* **49**, 871–875 (1978).
- Snaith, H. J. *et al.* Anomalous hysteresis in perovskite solar cells. *J. Phys. Chem. Lett.* **5**, 1511–1515 (2014).
- Sanchez, R. S. *et al.* Slow dynamic process in lead halide perovskite solar cells. Characteristic times and hysteresis. *J. Phys. Chem. Lett.* **5**, 2357–2363 (2014).
- Jeon, N. J. *et al.* Solvent engineering for high-performance inorganic–organic hybrid perovskite solar cells. *Nature Mater.* **13**, 897–903 (2014).

Acknowledgements

This work was supported by National Research Foundation of Korea (NRF) grants, funded by the Ministry of Science, ICT & Future Planning (MSIP) of Korea under contracts nos. NRF-2010-0014992, NRF-2012M1A2A261721, NRF-2012M3A7B4049986 (Nano Material Technology Development Program) and NRF-2012M3A6A7054861 (Global Frontier R&D Program on Center for Multiscale Energy System). MG acknowledges an Advanced Research Grant (ARG 247404) from the European Research Council (ERC), funded under the ‘Mesolight’ project.

Author contributions

N.G.P. conceived the experiments, performed data analysis and prepared the manuscript. J.H.I. and I.H.J. prepared materials, fabricated devices and characterized device structure and performance. M.G. analysed optical and IPCE data and edited the manuscript. N.P. measured light-harvesting efficiency and photo-CELIV. All authors discussed the results and commented on the manuscript.

Additional information

Supplementary information is available in the online version of the paper. Reprints and permissions information is available online at www.nature.com/reprints. Correspondence and requests for materials should be addressed to M.G. and N.G.P.

Competing financial interests

The authors declare no competing financial interests.